ACS Photonics

pubs.acs.org/journal/apchd5

Article

Inkjet Printing of Structurally Colored Self-Assembled Colloidal Aggregates

Pavel Yazhgur,* Nicolas Muller, and Frank Scheffold*

Cite This: *ACS Photonics* 2022, 9, 2809−2816

Read Online

ACCESS | Metrics & More | Article Recommendations | Supporting Information

ABSTRACT: Structurally colored materials offer increased stability, high biocompatibility, and a large variety of colors, which can hardly be reached simultaneously using conventional chemical pigments. However, for practical applications, such as inkjet printing, it is vital to compartmentalize these materials in small building blocks (with sizes ideally below 5 μm) and create "ready-to-use" inks. The latter can be achieved by using photonic balls (PB): spherical aggregates of nanoparticles. Here, we demonstrate, for the first time, how photonic ball dispersions can be used as inkjet printing inks. We use solvent drying techniques to manufacture structurally colored colloidal aggregates. The as-fabricated photonic balls are dispersed in pentanol to form ink. A custom-made inkjet printing platform equipped with an industrial printhead and recirculation fluidic system is used to print complex structurally colored patterns. We increase color purity and suppress multiple scattering by introducing carbon black as a broadband light absorber.

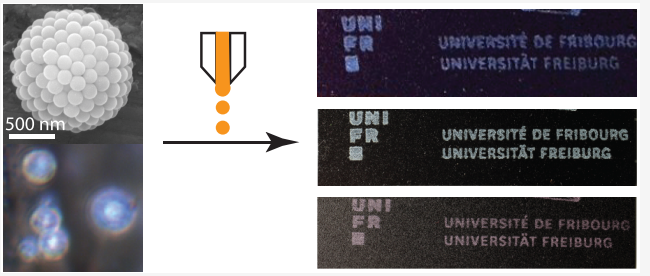

KEYWORDS: *photonic materials, structural color, inkjet printing, colloidal assembly*

1. INTRODUCTION

Over the past decade, researchers have made tremendous progress toward the understanding of stable structural coloration both from crystalline and noncrystalline materials.[1,2] The latter are essential since they provide noniridescent color similar to conventional dyes and are thus often preferred. Furthermore, structural colors do not age, contain no chemical pigments, stay ultraresistant to bleaching, and can be manufactured from low toxic or even edible materials, thus having much lower environmental and human health impacts. However, the delivery or deposition of the structural color materials remains a significant hurdle toward practical applications such as graphical printing. In addition, conventional drop-casting or spray-coating techniques have limited spatial resolution, and the resulting optical properties are challenging to control.

Inkjet printing proposes a more flexible color deposition strategy with high resolution. So far, the primary approach in fabricating structural colors using inkjet printing consists in jetting nanoparticle dispersions and drying them directly on the substrate.[3−6] After drying, the nanoparticles self-assemble in opal structures revealing structural color. This approach, however, strongly limits the range of available substrates. It also often requires substrate pretreatment.[6,7] Depending on the substrate hydrophobicity, different morphologies, including large-area films, thin film dots, or microdomes, can be printed.[5,8−11] The printing process has to be adapted to avoid the coffee-ring effect.[12] Furthermore, the necessity to dry droplets containing nanoparticles directly on the substrates limits the resolution and complicates color mixing.

Previous work has shown that one can confine nanoparticles inside emulsion droplets to produce clusters of photonic crystals and glasses, often named "photonic balls" (PB). Indeed, photonic balls contaning a larger number of nanoparticles can be efficiently fabricated using various colloidal assembly approaches. One can suspend the PBs in a solvent phase and then use the obtained colored ink for practical applications. Commonly, PBs with sizes in the tens of micrometer range are employed.[13−21] To enhance color purity and suppress white appearance, broadband light absorbers are often incorporated inside PBs.[19,22]

PB-based inks, however, have never been tested before for inkjet printing applications. The lack of studies is likely related to standard inkjet-printing technology's substantial pigment size limitations. The nozzles of industrial printheads range from 10 to 50 μm, meaning that the acceptable pigment size to reliably jet is around 1−5 μm. This tiny pigment size demands rigorous pigment dispersion optimization to keep high color performance and jettability. Here we demonstrate prefabricat-

Received: April 26, 2022
Published: August 2, 2022

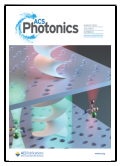

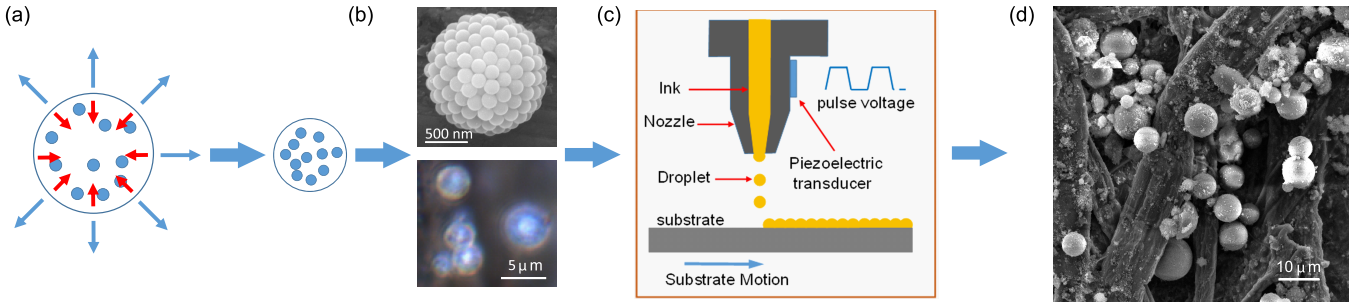

Figure 1. Schematic representation of the photonic-ink fabrication and inkjet printing. (a) Fabrication of photonic balls (PBs) by solvent drying: polystyrene nanoparticles (NPs) in water are emulsified in decanol. Due to the finite solubility of water in decanol, the droplets shrink, resulting in solid PBs. (b) SEM image of a dried PB and similar size PB dark field image. The nanoparticle diameter is d_{NP} = 180 nm in both cases. (c) Inkjet printing of preformulated inks. (d) SEM image of a paper with PBs after inkjet printing.

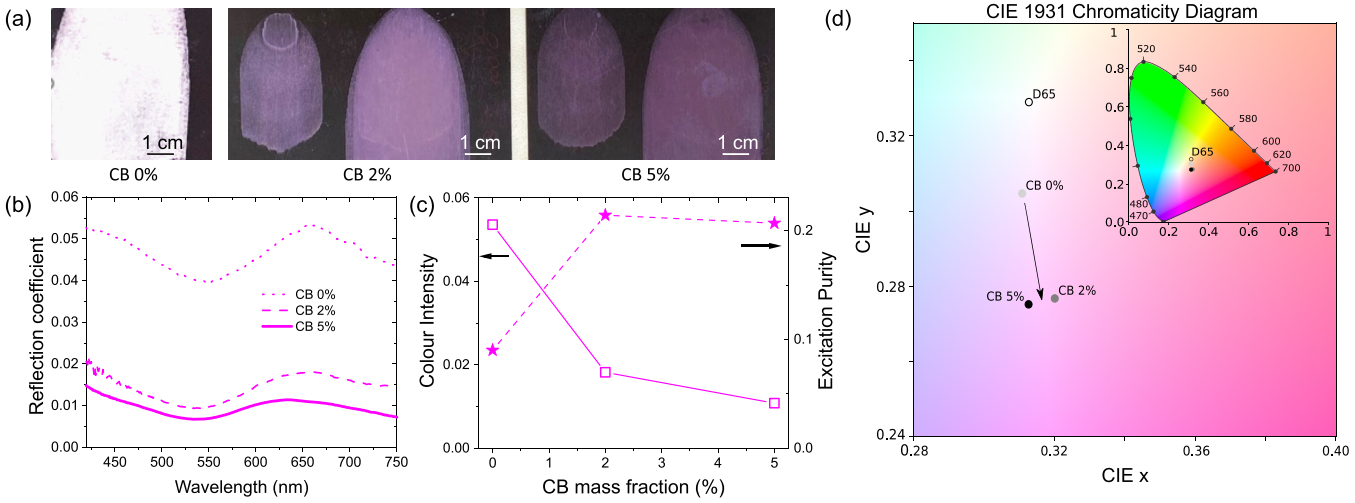

Figure 2. Structural color optimization. (a) Pictures of photonic ball films (PB mean diameter, 1.5 μm, NP diameter, d_{NP} = 270 nm) prepared with a thin film applicator for different concentrations of carbon black (CB) in the PBs (wt % of carbon black in dried photonic balls). (b) Reflection spectra of photonic balls films for different CB concentrations. The measured reflection coefficient is well below one due to the objective lens's numerical aperture (NA = 0.25). (c) Color intensity (height of the structural color peak at λ = 650 nm) and excitation purity for different CB concentrations. (d) CIE 1931 chromaticity diagram (CIE 1931 2° Standard Observer) showing chromatic coordinates of the CIE standard illuminant D65 and PB samples with various CB content. The graph shows a zoom around the experimental points, and the inset represents the whole chromaticity diagram.

ing of such structurally colored entities for later printing. We separate the PBs ink fabrication and the inkjet printing to achieve high flexibility. We print red, green, and blue colors by tuning the nanoparticle size appropriately. We demonstrate that various substrates, including black office paper, can be used without special pretreatment. Thus, the formulated inks can be used in commercially available inkjet printers without additional preparation.

2. RESULTS AND DISCUSSION

We prepare a suspension of PBs in decanol using solvent drying techniques, Figure 1. To this end, we produce a large quantity of polystyrene PBs ink with ball mean diameters D_{PB} below 10 μm. We chose polystyrene NPs with diameters, d_{NP}, equal to 270, 206, and 180 nm to target red, green, and blue colors (RGB). Small nanoparticle polydispersity (<5% as revealed by scanning electron microscopy (SEM)) is essential for creating bright colors. Furthermore, the strong negative charge of individual nanoparticles (zeta potential around −40 mV) ensures PB dispersions' stability. We prepare a batch with a mean diameter of approximately $D_{PB} \approx 1.1-1.4$ μm and a PB-polydispersity of 30−45% (see SI for particle size distributions). Each PB contains $N \approx 50-200$ nanoparticles per PB, depending on nanoparticle size. Despite their modest size, the individual PBs already demonstrate bright structural coloring, as shown in dark-field microscopy (Figure 1b). As explained previously,[23,24] an aggregation number $N \geq 100$ is sufficient to create a structure factor peak due to short-range order, comparable to the one found in infinite size photonic glasses ($N \rightarrow \infty$). We purified the fabricated PBs by centrifugation and redispersed them in pentanol. We use pentanol as a solvent due to its mixed polar/nonpolar character ensuring dispersion stability and its low viscosity η = 4 cP, surface tension γ = 25.5 mN/m, and drying time (boiling temperature 137 °C). We use the as-formulated photonic ink to create colored homogeneous films and complex printouts, either by thin-film casting or graphical inkjet printing.

To evaluate the color formation and optimize the ink formulation, we deposit thin homogeneous films of PBs with 270 nm nanoparticles utilizing a thin-film spreader. An example of such a film is shown in Figure 2a. The film appears white with a reddish color hue. From mass conservation, we can estimate the "effective" thickness of these films to be around 2 μm, comparable to the PB diameter. A closer look at the film

https://doi.org/10.1021/acsphotonics.2c00627
ACS Photonics 2022, 9, 2809−2816

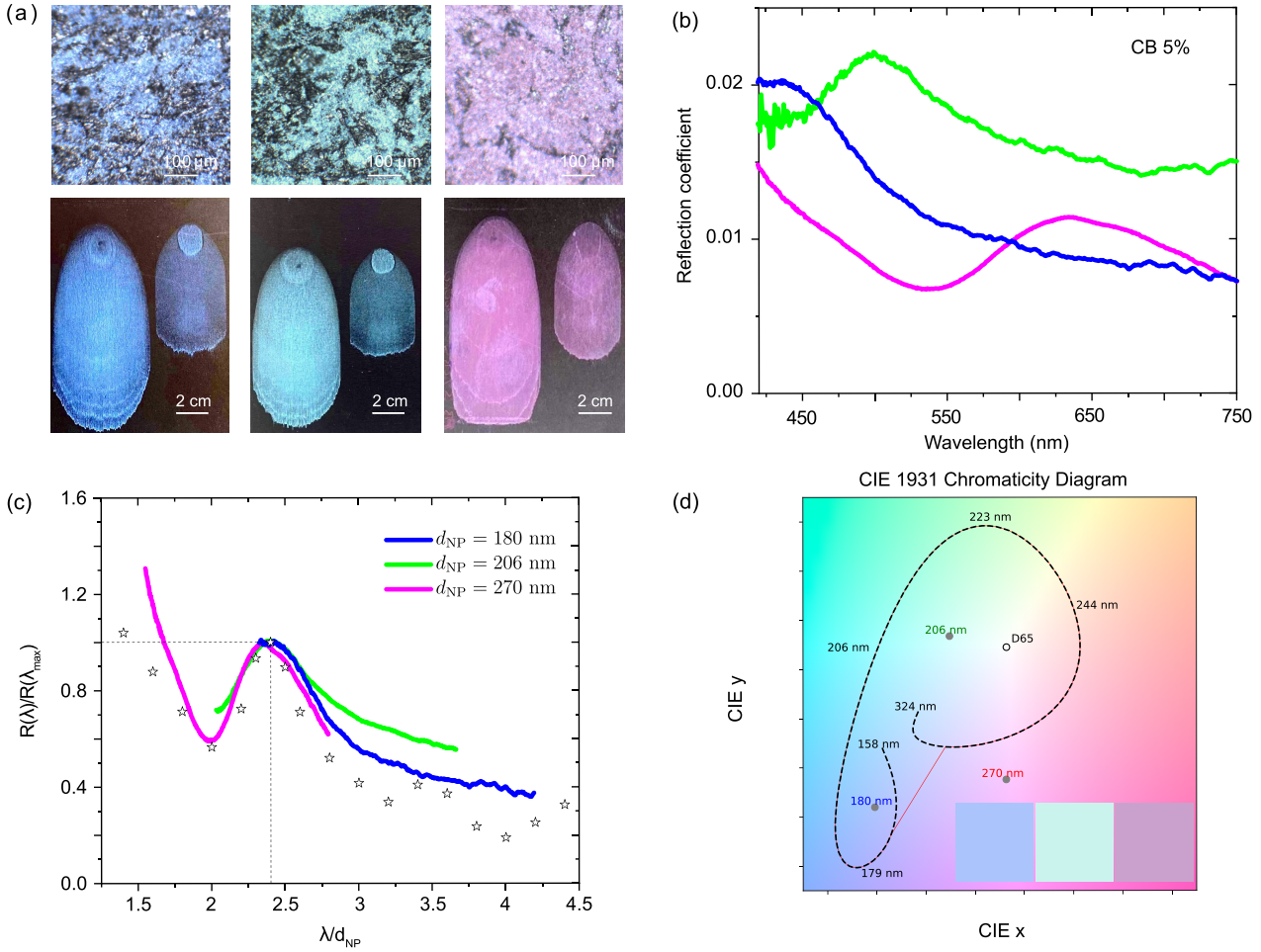

Figure 3. (a) Microscopy images and photos of PB films. (b) Reflection spectra of films made from PBs with differently sized nanoparticles: d_{NP} = 180 nm for the blue color, d_{NP} = 206 nm for green, and d_{NP} = 270 nm for red. (c) Normalized reflection coefficients and T-matrix calculation for backscattering intensity of a single PB with aggregation number N = 87. (d) CIE chromaticity diagram (CIE 1931 2° Standard Observer). The gray points show the experimental data, and the dashed black line represents the T-matrix prediction for various nanoparticle diameters. The red line represents the available gamut defined as an envelope around simulated data. Inset: colors calculated using experimental reflection spectra shown in (b).

structure reveals that, instead of fixed-thickness monolayers, the PB suspensions dry in separated concentrated regions (see SEM image, Figure 1d, and microscopy image, Figure 3a). These distinct regions, however, cannot be observed by a naked eye; the film appears homogeneous with some mm-scale density variations, Figure 2a. Spectrally resolved reflection reveals a peak intensity around 650 nm, significantly obscured by the white background (see Figure 2b). The observed whiteness is related to multiple light scattering of light, propagating in and between different PBs in the film, as discussed in ref 23. The typical scattering mean free path for a dense disordered packing of spheres for a wavelength near the reflection peak is around 1−3 μm, comparable to the PB size. To enhance color features and decrease multiple scattering and whiteness, we add the broadband absorber carbon black (CB) to the formulation[25] during PB assembly. Multiply scattered photons travel longer distances inside the material and are absorbed preferentially. As a result, the background light intensity decreases while the single scattering reflection peak and its position remain unchanged. In our experiments, we have compared PB-formulations containing 2 and 5 wt % of carbon black. From previous studies[25] we know that these concentrations give absorption lengths around 1.5 and 0.5 μm, comparable to the scattering mean free path inside a PB. By removing most of the multiple scattering background, we obtain colorful films as shown in Figure 2a. We use the measured reflection spectra to calculate the chromaticity coordinates xy and plot them on the CIE 1931 (Commission Internationale de L'Eclairage) chromaticity diagram. By adding CB, we move from the central white point, defined using CIE standard illuminant D65, to more saturated colors keeping the hue, as shown in Figure 2d. We obtain a magenta hue instead of pure red since the reflected intensity increases again in the blue visible spectral range. This rise at low wavelengths is known to exist (e.g., also for photonic glasses) and has been related to the backscattering from individual NPs.[26] This effect is not essential for green and blue colors since the uprise is shifted into the invisible UV spectral range, but it prevents us from creating pure red structural colors. In future studies, one can overcome this problem by mixing chemical and structural colors, for example, by adding substances absorbing blue light, or by changing the PB-structure through, for example, the use of core−shell primary nanoparticles[26] or other optimized photonic structures such as dielectric networks[27] or inverted photonic glasses.[28]

https://doi.org/10.1021/acsphotonics.2c00627
ACS Photonics 2022, 9, 2809−2816

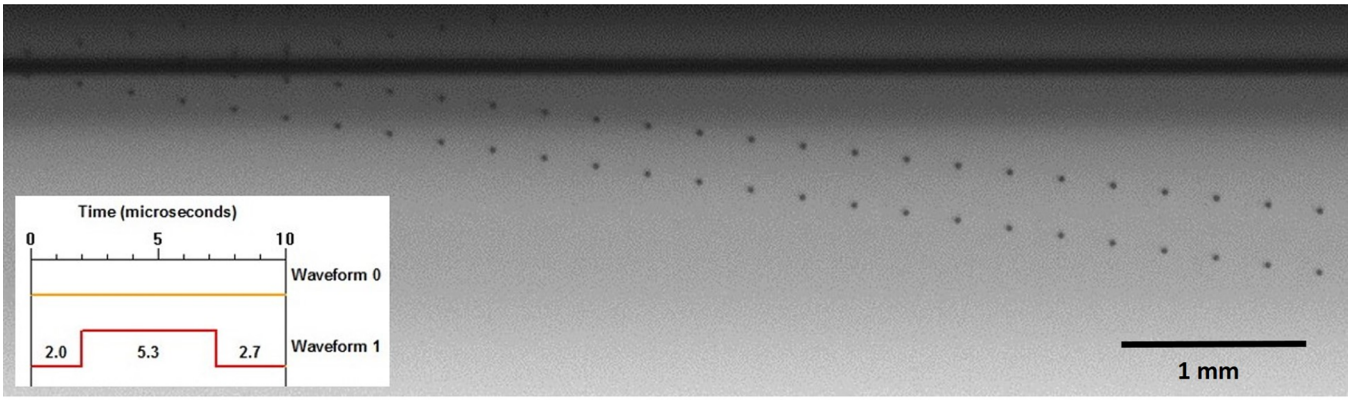

Figure 4. Dropwatching performed with an optimized waveform. Note that the image is obtained by stroboscopically illuminating the drops with a LED that emits light at the printhead's jetting frequency. The nozzles fire with a slight delay concerning each other to visualize the drop evolution after their ejection from the nozzle plate. The excitation voltage was set to 23 V, resulting in the generation of two drops of 9 pL each per pulse. The printhead operates at a native resolution of 360 dpi and possesses four nozzle rows (only one of which is in focus during drop watching), thus the distance between drops ejected from adjacent nozzles is 282 μm. The inset shows the applied voltage waveform for one excitation pulse during the stages of waiting (wavefront 0) and printing (waveform 1). Note that one excitation pulse yields two drops of equal volume. The height of the central excitation plateau can be parametrically varied to avoid satellites, change the drop speed, and thus achieve optimal jetting performance.

The chromaticity diagram also allows us to access the excitation purity p_e. The latter represents the relative distance of the chromaticity coordinates from the white point and can vary from 0 (pale color) to 1 (pure color). As shown in Figure 2c, adding CB increases the excitation purity until it saturates. In the meantime, the color intensity, defined as the reflection coefficient at peak position λ = 650 nm, goes down with the addition of CB. The latter shows that the contribution of broadband multiple scattering reflections decreases when adding CB. Tuning the amount of CB added naturally allows creating of colors with controlled purity, as illustrated in the chromaticity diagram, Figure 2d. In the following, we retain the CB mass fraction at 5% and thus keep the color purity constant. We have deposited films for three different colors as shown in Figure 3. The spectral reflectance measurements confirm the structural origin of the color. By using diameters 180 nm, 206 and 270 nm nanoparticles, the reflection peak position moves from 430 and 500 nm to 640 nm, respectively. The data suggest an approximate ratio between the NP diameter and the wavelength of the reflection peak as $\lambda_{max}/d_{NP} \sim 2.3-2.4$. The latter perfectly agrees with simple theoretical considerations based on single scattering. Indeed, for a disordered dense packing of spheres the structure factor peak is located around $q_{max} \simeq 2.3\pi/d_{NP}$.[29] For the backscattering direction, the maximum reflection is at $\lambda_{max} = 4\pi/q_{max}n_{eff}$, where n_{eff} is the effective refractive index of the media. By assuming Maxwell−Garnett effective medium refractive index $n_{eff} \approx 1.33$, this finally translates to $\lambda_{max}/d_{NP} \approx 1.74n_{eff} \approx 2.3$.

The reflectance data can be collapsed on a master curve, normalizing the reflection coefficient $R(\lambda)$ by the color peak intensity $R(\lambda_{max})$ and plotting the data as a function of dimensionless wavelength λ/d_{NP}, as shown in Figure 3c. Near structural isotropy and random orientation of PBs guarantees us the noniridescent color response. In the SI, we demonstrate a weak angular dependence of PB structural colors.

Next, we compare our reflection measurements with numerical calculations based on the multiple-sphere T-matrix method (MSTM). To this end, we generate a photonic ball using a molecular dynamics-based algorithm, taking into account the NP polydispersity, for details see ref 23. We obtain the angular dependent intensity scattered by a single PB, that is, the differential scattering cross-section $d\sigma(\theta, \lambda)/d\Omega$. This allows us to define the backscattering cross-section as $\sigma_{BS}(\lambda)$

$$\sigma_{BS}(\lambda) = 2\pi \int_{\theta_{min}}^{\theta_{max}} \frac{d\sigma(\theta, \lambda)}{d\Omega} \sin(\theta)\, d\theta \quad (1)$$

where the integration limits θ_{min} and θ_{max} are determined by the numerical aperture of microscope objective lenses. In such a single scattering model for structural coloration, the above-defined backscattering cross-section $\sigma_{BS}(\lambda)$ is proportional to the reflection spectrum $R(\lambda)$; see also refs 26 and 30. This allows us to estimate the normalized reflection coefficient as $R(\lambda)/R(\lambda_{max}) = \sigma_{BS}(\lambda)/\sigma_{BS}(\lambda_{max})$. Comparing experiment and theory, we assume that the addition of CB suppresses multiple scattering, but does not affect the photonic ball single scattering function. We find the numerical data in good agreement with the experimental data, especially near the reflection peak, Figure 3c. PB-polydispersity can explain differences between experiments and calculations at higher wavelengths.[23]

Based on the excellent agreement between numerical calculations and experiment, we can numerically predict a gamut of potentially available colors, as shown in Figure 3d. To this end, we vary the nanoparticle diameter d_{NP} in our simulations from 158 to 326 nm. This allows us to move the color peak position from 380 to 780 nm. The resulting chromaticity coordinates, shown by a dashed black line in Figure 3d, start in the blue part of the spectrum, pass through green and magenta, and go back to blue hues, but with lower excitation purity. The blue appearance for large nanoparticle sizes is due to the secondary peak. We note that the prediction line passes very close to the white point for red hues. It is challenging to create pure red colors using densely packed nanoparticle assemblies as shown by previous studies.[26] In the inset of Figure 3d we demonstrate the colors calculated from the experimental reflection spectra. Visually, they are very close to the ones observed in the printed films and images, showing the consistency between our measurements and calculations. As shown in Figure 2, without adding CB, multiple scattering decreases the color purity (i.e., moving in the direction of D65) while retaining the same hue. This allows us to estimate

https://doi.org/10.1021/acsphotonics.2c00627
ACS Photonics 2022, 9, 2809−2816

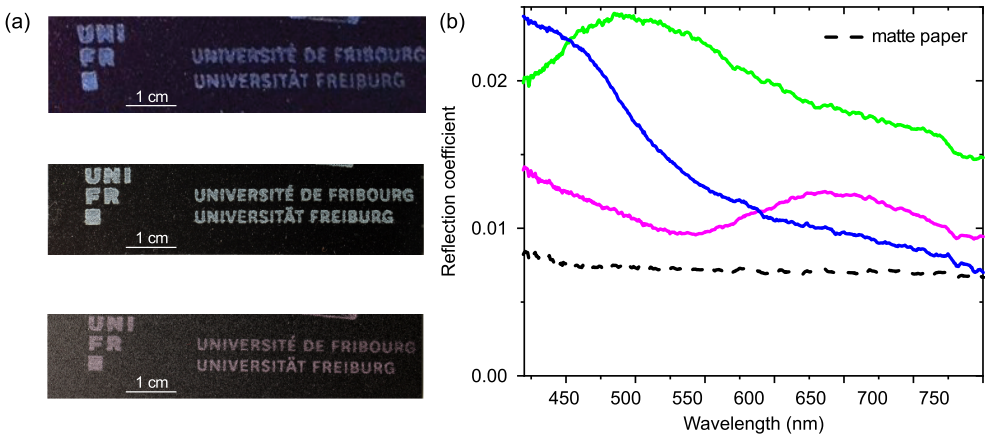

Figure 5. (a) Photos of inkjet-printed business cards featuring complex structurally colored patterns of the author's affiliation. (b) Reflection spectra of the inkjet-printed PB films. Dashed line, reflection signal from the black paper substrate. The University of Fribourg logo is reprinted with permission.

the available gamut as an envelope around the calculated curve. This gamut is shown by the thin red line in Figure 3d. We predict that any point inside this gamut can be reached by changing the nanoparticle size and the amount of multiple scattering, for example, by controlling the absorption length or thickness of PB films. Excessive amounts of the black absorber or preparing thin films will lead to purer colors on the edge of the predicted gamut. Both will, however, enormously decrease the color intensity. We note that the magenta sample shows higher color purity than expected from the simulations due to the increased reflection at low wavelengths. The increase is more substantial in the experiment than in simulations due to the remaining multiple scattering contribution. Interestingly, in this case, multiple scattering creates higher purity colors than what one can expect from the single scattering model. The deposited film color shows high stability to external factors, such as a humidity (see SI for more detail).

We use optimized ink formulations for inkjet printing with a professional Seiko RC1536-L printhead jetting micrometer-sized particles at a native resolution of 360 dpi. We employ a custom-built inkjet printer with constant ink recirculation. The latter is essential as micrometer-sized particles tend to sediment or agglomerate, thus clogging the nozzles or the printhead's fluidic channels. Furthermore, we use relatively dilute PB dispersions (0.4% volume fraction) to prevent clogging. Using an optimized waveform of the applied current driving the piezoelectric actuators of the printhead, we achieve stable drop formation without satellites, as shown in Figure 4. Under optimized settings, the as-formulated PB inks are jettable, and we proceeded to print tests. First, we program complex printing patterns containing fine lines to assess the overall printing quality. Next, we printed 10 subsequent layers as the PBs concentration in the formulation was relatively low. We require a minimum density of PBs to obtain coverage and photonic coloration. We employed a dwell time of 1 min between each of the 10 printing steps to allow each layer to dry. Figure 5 shows some of the as-obtained prints. In the SI, we additionally demonstrate how the PB coverage and color response develop with an increasing number of printed layers. Our results demonstrate the high quality of complex colored patterns of directly printed PB pigments. We furthermore found that other substrates are equally suitable for printing without pretreatment (see SI); however, the black paper shown in Figure 5 gives the best color performance.

3. CONCLUSIONS AND OUTLOOK

We have demonstrated the fabrication of micrometer-sized PB pigments that give structural coloration. Incorporating carbon black (CB) as a broadband light absorber suppresses undesired multiple scattering. Adding CB drastically increases the color excitation purity while at the same time reducing the color intensity. This allows us to create red, green, and blue colorful films. We have used electromagnetic simulations to predict the full gamut of available colors. Furthermore, we disperse the PBs in pentanol, forming a stable dispersion. We adapted the formulation's rheological parameters to fit the specifications of a state-of-the-art industrial printhead. Using a custom-built inkjet printer with recirculation, we printed high-quality test patterns for red, green, and blue PBs. To optimize the drop formation, we adjusted the waveform of the print head driving current and performed drop-watching experiments. To avoid clogging the printhead, we worked with a dilute ink formulation of less than 1% PB volume fraction. Consequently, we need multiple passes to obtain sufficient PB coverage of the substrate. Increasing the PBs concentration for printing in a single pass without clogging the printhead requires further optimization steps. In our experiments, large PBs in the polydisperse distribution's tail can lead to clogging. Therefore, we could only jet formulations with a PB mean diameter of 1.1−1.4 μm. We plan to study the effect of mixing PBs in different ratios using inkjet technology in future work. We argue that an optimized internal structure of the primary NP or PB, for example, based on a network or core−shell architecture, should improve red-color performance.

4. EXPERIMENTAL SECTION

4.1. Nanoparticle Synthesis and Photonic Ball Assembly. We synthesize polystyrene nanoparticles (NPs) using standard surfactant-free polymerization using 4-vinylbenzenesulfonate as an ionic comonomer and methanol as a cosolvent. By varying the methanol content, we could obtain NPs of different sizes. Scanning electron microscopy SEM (Tescan Mira3 LM FE) determines the mean diameter of the spheres to be 180, 206, and 270 nm, with a polydispersity of approximately 5% (from SEM measurements).

Using these NPs, we fabricate photonic balls (PB) by solvent-drying. To this end, we add about 1 mL of aqueous NP-dispersion, at 1% volume fraction, to 50 mL of anhydrous

https://doi.org/10.1021/acsphotonics.2c00627
ACS Photonics 2022, 9, 2809−2816

decanol. We pass the mixture through a narrow constriction using two syringes to make small PBs (mean PB diameter ≃ 1.1−1.4 μm). Since water is slightly soluble in decanol, the droplets rapidly shrink, leading to solid PBs. Finally, we purify PB dispersions by centrifugation and redisperse PBs in pentanol. We determine the mean size and the particle size distribution (PSD) from image analysis based on scanning electron microscopy (SEM). For most formulations, we add carbon black (Vulcan XC72R, Cabot corporation, absorption spectra in SI), typically 5 wt % in water using 1 wt % Tween 20 (Sigma-Aldrich) as a stabilizer, to the polystyrene aqueous nanoparticle dispersion before emulsification.

The formulated PB dispersions in pentanol slowly sediment on a time scale of hours. Though they can be reversibly redistributed by shaking or stirring, we use freshly prepared samples (1−2 days old) to avoid any potential impediments.

4.2. Optical Characterization. We measure reflection spectra in a bright field configuration using a Zeiss Axio Scope.A1 (Zeiss AG, Oberkochen, Germany) light microscope using Zeiss, EC Epiplan-Neofluar ×10, NA = 0.25 objective, and halogen lamp (Zeiss HAL100) light source in Koehler illumination. This allows us to collect reflected light from θ_{min} = 165° to θ_{max} = 180°. The reflected light is collected by an optical fiber (Ocean optics, QP230−2-XSR, 230 μm core) with a measurement spot size of ≈25 μm. We analyze the collected light with an Ocean Optics Maya2000 Pro spectrometer (Ocean Optics, Dunedin, FL, U.S.A.). We calibrate the spectra by measuring the reflectance of a mirror as a reference. Light microscopy images are acquired with a CCD camera from Point Grey (GS3-U3-28S5C-C, FLIR Integrated Imaging Solutions Inc., Richmond, Canada). We use a white standard (Spectralon) to calibrate the white balance. We took photographs of the PB films using a DSLR camera Canon EOS 200D and white paper as a white standard.

4.3. Numerical Calculations. We employ the multiple-sphere T-matrix method (MSTM open source code) to calculate numerically the differential scattering cross-section of densely packed assemblies of nanoparticles (PBs).[31,32] We generate the PB-structures used as input for the MSTM code by running a force-biased generation algorithm followed by a molecular dynamics equilibration using the PackingGeneration project,[33,34] as explained in ref 23. This algorithm supports polydisperse packings. To mimic the experimental conditions, we chose to work with a polydispersity of 5% with a filling fraction of φ = 0.60.

The CIE chromaticity diagrams and color excitation purities were calculated using freely available Colour Science python package.[35] To this end, the reflection spectra $R(\lambda)$ are converted to tristimulus X, Y, Z values using white illumination spectrum (CIE Standard Illuminant D65) $I(\lambda)$ and CIE 1931 2° Standard Observers color matching functions $\overline{x}(\lambda)$, $\overline{y}(\lambda)$, and $\overline{z}(\lambda)$ for primary colors:

$$X = \frac{1}{N}\int_{\lambda} R(\lambda)I(\lambda)\overline{x}(\lambda)\ \mathrm{d}\lambda \tag{2}$$

$$Y = \frac{1}{N}\int_{\lambda} R(\lambda)I(\lambda)\overline{y}(\lambda)\ \mathrm{d}\lambda \tag{3}$$

$$Z = \frac{1}{N}\int_{\lambda} R(\lambda)I(\lambda)\overline{z}(\lambda)\ \mathrm{d}\lambda \tag{4}$$

where

$$N = \int_{\lambda} I(\lambda)\overline{y}(\lambda)\ \mathrm{d}\lambda \tag{5}$$

Tristumulus is then converted to normalized CIE xy space by $x = X/(X + Y + Z)$ and $y = Y/(X + Y + Z)$. This allow us to define color purity as

$$p_e = \sqrt{\frac{(x - x_n)^2 + (y - y_n)^2}{(x_I - x_n)^2 + (y_I - y_n)^2}} \tag{6}$$

where (x_n, y_n) corresponds to the white point and (x_I, y_I) corresponds to the intersection of the straight line connecting white and sample point with the perimeter of the chart. For Illuminant D65, the white point is (0.31271, 0.32902).

4.4. Film Spreading. We spread as-formulated PB inks on different substrates using a Zehntner ZAA 2300 Automatic thin-film applicator. For this purpose, we employ a 25 μm profile wire bar. PB inks (4% volume fraction of PB in pentanol) are drop-casted in intervals of 60 pl using a pipet. After each application, the drop is spread at a constant speed on the wire bar. The thin film spreading is performed at ambient conditions without heating the substrate.

4.5. Inkjet Printing. The Seiko RC1536-L was identified as the optimal printhead that fulfils all the requirements for jetting inks loaded with >1 μm sized pigments. This printhead operates at an intrinsic resolution of 360 dpi while possessing four jetting rows. In addition, this printhead allows for the recirculation of the ink, an essential feature since micrometre-sized pigments tend to sediment or even agglomerate, resulting in the rapid clogging of the nozzles and the printhead's fluidic channels. Therefore, the recirculation flow rate is set to 30 mL/min. In addition, the Seiko RC1536-L can operate with different solvents, and we identify no compatibility issues for pentanol used in this study. Dropwatching (DW) studies a drop's formation and temporal development once ejected from a printhead. Optimizing drop speed and avoiding satellites that deteriorate the overall printing quality is a necessary step to jet ink in a stable and reproducible manner. We perform DW at a 1 kHz repetition rate and can reach the acoustic optimum. The latter is the optimal holding time of the primary excitation plateau for which a maximal amount of energy can be transferred to a drop, thus increasing its velocity. The acoustic optimum is found to be 5.3 μs. The voltage applied to the piezoelectric actuators, responsible for the ejection of the ink in a printhead, is set to 23 V. These settings yield two well-defined drops, each of a volume of 9 pL and a speed of 6 m/s, without any satellites. Moreover, tickling the piezoelectric elements at the nozzle level avoids drying and sedimentation. The final waveform and the determination of the acoustic optimum are reported in the SI.

■ ASSOCIATED CONTENT

Supporting Information

The Supporting Information is available free of charge at https://pubs.acs.org/doi/10.1021/acsphotonics.2c00627.

PB size distribution, angular-resolved optical spectroscopy, humidity test, influence of printed layers number, substrate optimization, and details of waveform tuning (PDF)

https://doi.org/10.1021/acsphotonics.2c00627
ACS Photonics 2022, 9, 2809−2816

AUTHOR INFORMATION

Corresponding Authors

Pavel Yazhgur − *Department of Physics, University of Fribourg, CH-1700 Fribourg, Switzerland;* orcid.org/0000-0001-6809-6828; Email: pavel.yazhgur@unifr.ch

Frank Scheffold − *Department of Physics, University of Fribourg, CH-1700 Fribourg, Switzerland;* Email: frank.scheffold@unifr.ch

Author

Nicolas Muller − *iPrint Institute, HEIA-FR, HES-SO University of Applied Sciences and Arts Western Switzerland, Fribourg CH-1700, Switzerland*

Complete contact information is available at: https://pubs.acs.org/10.1021/acsphotonics.2c00627

Funding

The Swiss National Science Foundation financially supported this work through the National Center of Competence in Research Bio-Inspired Materials, No. 182881 and through Project Nos. 188494, 183651, and 197146. N.M. acknowledges the financial support of the HES-SO through the Project Structural Pigments.

Notes

The authors declare no competing financial interest.

ACKNOWLEDGMENTS

P.Y. thanks Geoffroy Aubry for the help with T-matrix calculations and Viola Bauernfeind for the help with angle-resolved spectroscopy.

REFERENCES

(1) Braun, P. V. Colour without colourants. *Nature* **2011**, *472*, 423−424.

(2) Hwang, V.; Stephenson, A. B.; Barkley, S.; Brandt, S.; Xiao, M.; Aizenberg, J.; Manoharan, V. N. Designing angle-independent structural colors using Monte Carlo simulations of multiple scattering. *Proc. Natl. Acad. Sci. U. S. A.* **2021**, *118*, e2015551118.

(3) Park, J.; Moon, J.; Shin, H.; Wang, D.; Park, M. Direct-write fabrication of colloidal photonic crystal microarrays by ink-jet printing. *J. Colloid Interface Sci.* **2006**, *298*, 713−719.

(4) Wang, L.; Wang, J.; Huang, Y.; Liu, M.; Kuang, M.; Li, Y.; Jiang, L.; Song, Y. Inkjet printed colloidal photonic crystal microdot with fast response induced by hydrophobic transition of poly (N-isopropyl acrylamide). *J. Mater. Chem.* **2012**, *22*, 21405−21411.

(5) Nam, H.; Song, K.; Ha, D.; Kim, T. Inkjet printing based monolayered photonic crystal patterning for anti-counterfeiting structural colors. *Sci. Rep.* **2016**, *6*, 30885.

(6) Echeverri, M.; Patil, A.; Hu, Z.; Shawkey, M. D.; Gianneschi, N. C.; Dhinojwala, A. Printing a Wide Gamut of Saturated Structural Colors Using Binary Mixtures, With Applications in Anticounterfeiting. *ACS Appl. Mater. Interfaces* **2020**, *12*, 19882−19889.

(7) Ko, H.-Y.; Park, J.; Shin, H.; Moon, J. Rapid self-assembly of monodisperse colloidal spheres in an ink-jet printed droplet. *Chemistry of materials* **2004**, *16*, 4212−4215.

(8) Cui, L.; Li, Y.; Wang, J.; Tian, E.; Zhang, X.; Zhang, Y.; Song, Y.; Jiang, L. Fabrication of large-area patterned photonic crystals by ink-jet printing. *J. Mater. Chem.* **2009**, *19*, 5499−5502.

(9) Shanker, R.; Sardar, S.; Chen, S.; Gamage, S.; Rossi, S.; Jonsson, M. P. Noniridescent Biomimetic Photonic Microdomes by Inkjet Printing. *Nano Lett.* **2020**, *20*, 7243−7250.

(10) Hu, Z.; Bradshaw, N. P.; Vanthournout, B.; Forman, C.; Gnanasekaran, K.; Thompson, M. P.; Smeets, P.; Dhinojwala, A.; Shawkey, M. D.; Hersam, M. C.; et al. Non-Iridescent Structural Color Control via Inkjet Printing of Self-Assembled Synthetic Melanin Nanoparticles. *Chem. Mater.* **2021**, *33*, 6433−6442.

(11) Wu, Y.; Ren, J.; Zhang, S.; Wu, S. Nanosphere-aggregation-induced reflection and its application in large-area and high-precision panchromatic inkjet printing. *ACS Appl. Mater. Interfaces* **2020**, *12*, 10867−10874.

(12) Park, J.; Moon, J. Control of colloidal particle deposit patterns within picoliter droplets ejected by ink-jet printing. *Langmuir* **2006**, *22*, 3506−3513.

(13) Park, J.-G.; Kim, S.-H.; Magkiriadou, S.; Choi, T. M.; Kim, Y.-S.; Manoharan, V. N. Full-Spectrum photonic pigments with non-iridescent structural colors through colloidal assembly. *Angew. Chem., Int. Ed.* **2014**, *53*, 2899−2903.

(14) Moon, J. H.; Yi, G.-R.; Yang, S.-M.; Pine, D. J.; Park, S. B. Electrospray-Assisted Fabrication of Uniform Photonic Balls. *Adv. Mater.* **2004**, *16*, 605−609.

(15) Wang, J.; Zhu, J. Recent advances in spherical photonic crystals: Generation and applications in optics. *European polymer journal* **2013**, *49*, 3420−3433.

(16) Yi, G.-R.; Jeon, S.-J.; Thorsen, T.; Manoharan, V. N.; Quake, S. R.; Pine, D. J.; Yang, S.-M. Generation of uniform photonic balls by template-assisted colloidal crystallization. *Synth. Met.* **2003**, *139*, 803−806.

(17) Kim, S.-H.; Jeon, S.-J.; Yi, G.-R.; Heo, C.-J.; Choi, J. H.; Yang, S.-M. Optofluidic assembly of colloidal photonic crystals with controlled sizes, shapes, and structures. *Advanced materials* **2008**, *20*, 1649−1655.

(18) Xiao, M.; Hu, Z.; Wang, Z.; Li, Y.; Tormo, A. D.; Le Thomas, N.; Wang, B.; Gianneschi, N. C.; Shawkey, M. D.; Dhinojwala, A. Bioinspired bright noniridescent photonic melanin supraballs. *Science Advances* **2017**, *3*, e1701151.

(19) Ohnuki, R.; Sakai, M.; Takeoka, Y.; Yoshioka, S. Optical characterization of the photonic ball as a structurally colored pigment. *Langmuir* **2020**, *36*, 5579−5587.

(20) Vogel, N.; Utech, S.; England, G. T.; Shirman, T.; Phillips, K. R.; Koay, N.; Burgess, I. B.; Kolle, M.; Weitz, D. A.; Aizenberg, J. Color from hierarchy: Diverse optical properties of micron-sized spherical colloidal assemblies. *Proc. Natl. Acad. Sci. U. S. A.* **2015**, *112*, 10845−10850.

(21) Wang, J.; Sultan, U.; Goerlitzer, E. S.; Mbah, C. F.; Engel, M.; Vogel, N. Structural Color of Colloidal Clusters as a Tool to Investigate Structure and Dynamics. *Adv. Funct. Mater.* **2019**, *30*, 1907730.

(22) Han, S. H.; Choi, Y. H.; Kim, S.-H. Co-Assembly of Colloids and Eumelanin Nanoparticles in Droplets for Structural Pigments with High Saturation. *Small* **2022**, *18*, 2106048.

(23) Yazhgur, P.; Aubry, G. J.; Froufe-Pérez, L. S.; Scheffold, F. Light scattering from colloidal aggregates on a hierarchy of length scales. *Opt. Express* **2021**, *29*, 14367−14383.

(24) Yazhgur, P.; Aubry, G. J.; Froufe-Pérez, L. S.; Scheffold, F. Scattering phase delay and momentum transfer of light in disordered media. *Physical Review Research* **2022**, *4*, 023235.

(25) Forster, J. D.; Noh, H.; Liew, S. F.; Saranathan, V.; Schreck, C. F.; Yang, L.; Park, J.-G.; Prum, R. O.; Mochrie, S. G.; O'Hern, C. S.; et al. Biomimetic isotropic nanostructures for structural coloration. *Adv. Mater.* **2010**, *22*, 2939−2944.

(26) Magkiriadou, S.; Park, J.-G.; Kim, Y.-S.; Manoharan, V. N. Absence of red structural color in photonic glasses, bird feathers, and certain beetles. *Phys. Rev. E* **2014**, *90*, 062302.

(27) Bergman, M. J.; García-Astrain, C.; Fuchs, N.; Manne, K.; Yazhgur, P.; Froufe-Pérez, L. S.; Liz-Marzán, L. M.; Scheffold, F. Macroporous Silica Foams Fabricated via Soft Colloid Templating. *Small Methods* **2022**, *6*, 2101491.

(28) Kim, S.-H.; Magkiriadou, S.; Rhee, D. K.; Lee, D. S.; Yoo, P. J.; Manoharan, V. N.; Yi, G.-R. Inverse photonic glasses by packing bidisperse hollow microspheres with uniform cores. *ACS Appl. Mater. Interfaces* **2017**, *9*, 24155−24160.

(29) Liu, J.; Schöpe, H.-J.; Palberg, T. An Improved Empirical Relation to Determine the Particle Number Density of Fluid-Like

Ordered Charge-Stabilized Suspensions. *Particle & Particle Systems Characterization: Measurement and Description of Particle Properties and Behavior in Powders and Other Disperse Systems* **2000**, *17*, 206–212.
(30) Hwang, V.; Stephenson, A. B.; Magkiriadou, S.; Park, J.-G.; Manoharan, V. N. Effects of multiple scattering on angle-independent structural color in disordered colloidal materials. *Phys. Rev. E* **2020**, *101*, 012614.
(31) Mackowski, D.; Mishchenko, M. A multiple sphere T-matrix Fortran code for use on parallel computer clusters. *Journal of Quantitative Spectroscopy and Radiative Transfer* **2011**, *112*, 2182–2192.
(32) Mackowski, D. W. Multiple Sphere T Matrix Version 3.0. http://www.eng.auburn.edu/~dmckwski/scatcodes/, (accessed 2022–05–01).
(33) Baranau, V.; Tallarek, U. Random-close packing limits for monodisperse and polydisperse hard spheres. *Soft Matter* **2014**, *10*, 3826–3841.
(34) Baranau, V. PackingGeneration Version 1.0.1.28. DOI: 10.5281/zenodo.580324, (accessed 2022–05–01).
(35) Colour Science Version 0.3.16. https://www.colour-science.org/, (accessed 2022–05–01).

https://doi.org/10.1021/acsphotonics.2c00627
ACS Photonics 2022, 9, 2809–2816